Article

Probing Interactions at the Organic−Inorganic Interface of Biomass Burning Aerosol: Reactivity of Organic Tracer Species with Different Iron Oxide Mineral Phases

Published as part of ACS Earth and Space Chemistry special issue "Hartmut Hermann Festschrift".

Jane A. Sedlak, Manal Vishnoi, Kiefer Forsch, Pazinah Bhadha, Sarah M. Aarons, and Vicki H. Grassian*

Cite This: *ACS Earth Space Chem.* 2024, 8, 2463−2473

Read Online

ACCESS | Metrics & More | Article Recommendations | SI Supporting Information

ABSTRACT: As wildfire events become more frequent, there is a need to better understand the impact of smoke on the environment and human health. Smoke, or biomass burning aerosol (BBA), can undergo atmospheric processing changing its chemical and optical properties. We examined the interactions between four lignin pyrolysis products (catechol, syringol, syringic acid, and vanillic acid) and three BBA-relevant iron oxide mineral phases (hematite, maghemite, and magnetite) using attenuated total reflectance-Fourier transform infrared spectroscopy and dissolved iron measurements to better understand how atmospheric processing changes concentrations of soluble iron, iron oxidation state, and brown carbon abundance. Reductive dissolution was the primary dissolution mechanism for catechol and syringol, which led to a substantial amount of iron release ($p < 0.05$), whereas syringic and vanillic acids had little impact on dissolution. Comparisons with other BBA relevant compounds highlight the importance of both steric and electronic structures in the reductive dissolution process. The maghemite and magnetite phases, which are more likely to be present in BBA, released significantly more dissolved iron than hematite ($p < 0.05$), emphasizing the need to use BBA relevant iron oxide proxies in laboratory studies. This work provides insight into observations of iron dissolution and transformation of organics in BBA.

KEYWORDS: *biomass burning aerosol, iron oxide, mineral dust, wildfire smoke, atmospheric processing, lignin pyrolysis*
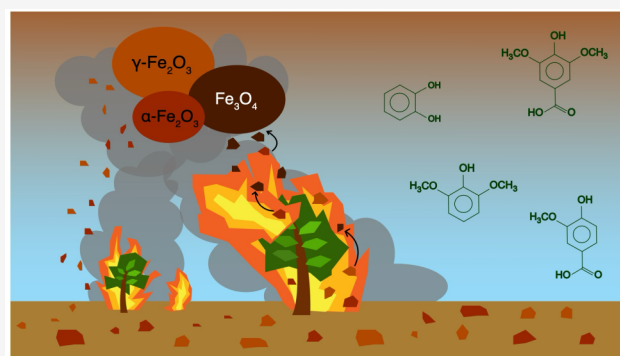
INTRODUCTION

While the air quality has improved in the United States since the enactment of the Clean Air Act in 1963, wildfires have the potential to reverse decades of progress in reducing anthropogenic particulate matter emissions.[1,2] Increased wildfire events and their determinantal effects on air quality and human health are not unique to the United States and these events are only expected to increase in frequency and size globally as the climate changes.[3,4] The emissions from wildfires, biomass burning aerosol (BBA), have some unique characteristics compared to other aerosols. In particular, BBA contains inorganic components, including elements derived from the crust whose size, morphology, and phase may be different from those of typical mineral dust sources, such as the Sahara Desert or eolian emissions from other desert regions.[5−7] BBA also contains several aromatic compounds that are less prevalent in the polluted troposphere, such as substituted phenols from lignin pyrolysis.[8]

Of the crustal elements in BBA, iron is of particular interest, given both its oxidative/reductive and nutrient properties. Deposition of aerosols present in wildfire smoke in nutrient-limited regions of the ocean has been linked to increased primary productivity, the scale of which cannot be fully explained.[9] Additionally, wildfire particulate matter has been shown to be more toxic compared to similarly sized aerosol.[10] The precise mechanism of wildfire toxicity remains unclear; however, metals such as iron may contribute to this enhanced toxicity through the generation of reactive oxygen species.[11,12] While morphology[5] and acidic processing[7,13−16] play a role in the enhanced solubility of iron in BBA and its corresponding environmental and health impacts, these factors alone cannot fully explain the highly soluble nature of iron in BBA.[14−19]
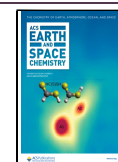
A majority of iron in BBA comes from the uplift of mineral dust from the land surface; however, the dust lofted by wildfire
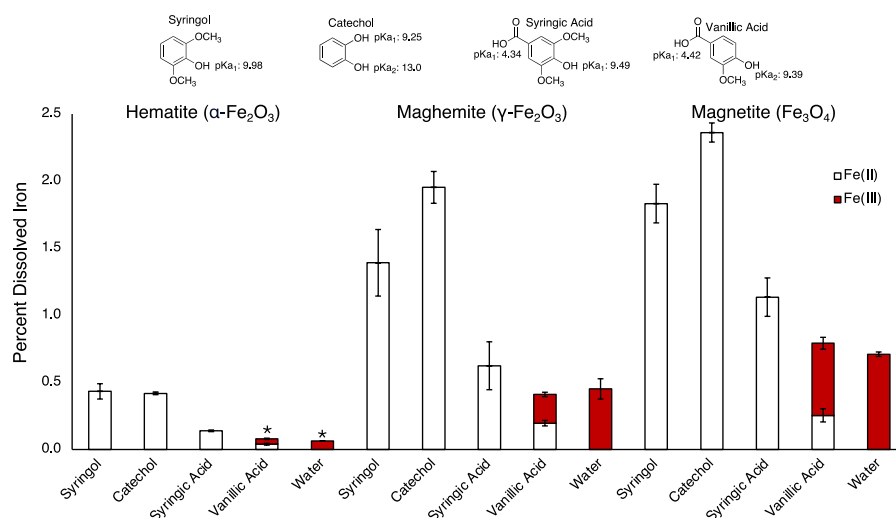
Figure 1. Percent dissolved iron, as determined by the ferrozine method, for each iron oxide mineral phase (loading: 0.5 mg/mL) in the presence and absence of different lignin pyrolysis products (0.2 mM) after 24 h at pH 2 (HCl). *Below LOQ. Organic structures and pK_a are also shown.[42,43]

smoke is not necessarily of identical composition as the dust lofted by strong winds.[20,21] For example, a recent study of ground ash after a fire at the wildland−urban interface found that a majority of the iron was present in the minerals magnetite and maghemite as opposed to more common soil mineral phases like hematite or goethite.[22] Ground ash from wildfires located away from the wildland−urban interface has also been shown to contain magnetite and maghemite after fires,[23,24] indicating the possibility of mineral phase changes during wildfire events. The presence of these less common iron oxide phases in high abundance may be due to phase changes resulting from the high temperatures and reducing environment of wildfires.[22] Despite the differences in phase between the iron oxides in BBA and those in soil, BBA-relevant phases remain understudied. Studies on how these phases react are key to developing a better understanding of BBA chemistry.

To date, the majority of laboratory studies of BBA-relevant systems have used hematite, Arizona Test Dust (AZTD), and/or dissolved iron (FeCl$_3$) as representative iron minerals.[25−29] In the reaction of catechol and guaiacol with Fe(III), the rapid formation of polymeric products has been observed.[25] Importantly, oxygen does not play a role in the polymerization of lignin pyrolysis products reacting with dissolved Fe(III).[30] However, there have been few observations of how BBA-relevant iron oxide mineral phases, such as magnetite and maghemite, interact and react with lignin pyrolysis products such as methoxyphenols.[30] The available studies directed toward understanding the interaction of lignin derivatives at iron interfaces have shown that lignin derivatives including hydroquinones, QH$_2$, promote the reductive dissolution of iron oxides, such as goethite, α-FeOOH, to give reduced iron and quinones (Q):

$$2\alpha\text{FeOOH}_{(s)} + \text{QH}_2 \rightarrow 2\text{Fe}^{2+} + \text{Q} + 4\text{OH}^- \tag{1}$$
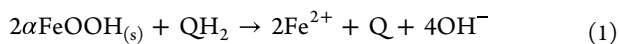
However, these studies may only partially inform our understanding of BBA given the lower pH regime that occurs in atmospheric aerosols, which may lead to different iron reaction pathways.[31]

To provide insight into iron chemistry in BBA, we investigated interfacial interactions of four BBA lignin pyrolysis products (catechol, syringol, syringic acid, and vanillic acid; see

Figure 1 for structures) with three different iron oxide mineral phases (hematite, maghemite, and magnetite) using attenuated total reflectance-Fourier transform infrared (ATR-FTIR) spectroscopy. All four compounds have been detected in biomass burning emissions, with syringol and syringic acid potentially serving as tracers for hardwoods and vanillic acid serving as a possible tracer for softwoods.[8] We also measured iron dissolution under acidic pH conditions to assess the role of these organic compounds in the dissolution processes under atmospherically relevant regimes. Overall, these results suggest that some BBA lignin pyrolysis products can lead to the release of substantial amounts of dissolved Fe(II) from the iron oxide mineral phases, which is relevant to our understanding of wildfire-derived nutrient delivery and utilization in the ocean.

■ EXPERIMENTAL METHODS AND MATERIALS

Materials. Hematite (α-Fe$_2$O$_3$, high purity 99.5+%, 30 nm, product ID: US3160), maghemite (γ-Fe$_2$O$_3$, high purity, 99.5+ %, 20 nm, product ID: US3200), and magnetite (Fe$_3$O$_4$, high purity, 99.5+%, 15 to 20 nm, product ID: US3230) were purchased from US Research Nanomaterials Inc. Iron oxide mineral phases used in this study were characterized (for surface area measurements and details regarding acid digestion, see Table S1; for pXRD, see Figure S1). Magnetite Fe(II) content was also determined (Figure S2). Additional material/sample details and data are provided in Supporting Information Sections S1.1 and 1.2.

The organic compounds used in this study were purchased from Sigma-Aldrich and used without further purification: catechol (ReagentPlus, ≥99%), syringol (2,6-dimethoxyphenol, 99%), vanillic acid (HPLC, purum, ≥97.0%), syringic acid (HPLC, ≥95%), resorcinol (ACS reagent, ≥99.0%), guaiacol (≥98.0%), and vanillin (ReagentPlus, 99%). Levoglucosan (>99%) was purchased from TCI. The solution pH was adjusted using 1 N hydrochloric acid and 1 N sodium hydroxide (Fisher).

ATR-FTIR Spectroscopy. ATR-FTIR spectroscopy was used to characterize interactions of the ligands with the three iron oxide phases. Experiments were carried out at both pH 2 and 7. The ATR-FTIR spectroscopic measurements were carried out using a Nicolet iS10 FTIR (Thermo-Fisher)
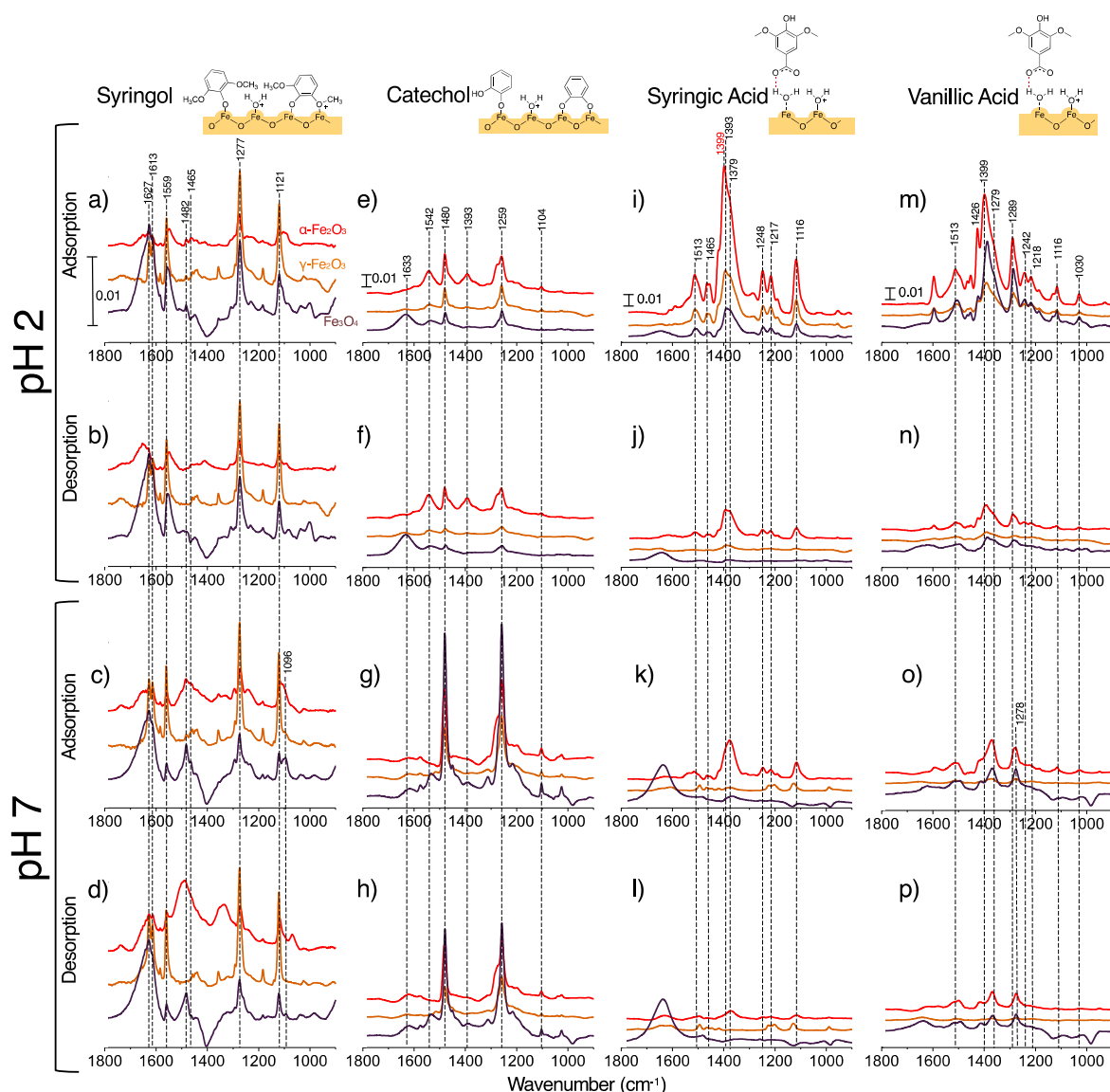
Figure 2. ATR-FTIR spectra for lignin pyrolysis products adsorbed on different iron oxide mineral phases (red: hematite, orange: maghemite, and brown: magnetite). After 100 min of flowing 1 mM solutions adjusted to either pH 2 (top spectra) or 7 (bottom spectra), adsorption spectra were collected. The desorption spectra were recorded following 30 to 60 min of flowing pH-adjusted water over the different iron oxide phases. Assigned and hypothesized surface complexes are shown at the top of each column.

spectrometer with a mercury cadmium telluride detector (MCT/A) detector and an Amorphous Material Transmitting IR Radiation (AMTIR) crystal in a Teflon-coated flow cell (PIKE Technologies) as previously described.[32−35] Briefly, the hematite and maghemite samples were heated at 220 °C for 12 h, while magnetite was not heated to avoid further oxidation of the sample (see Supporting Information Section S1.3 for a discussion of magnetite oxidation upon heating). Deionized water (1 mL) was added to 5 mg of the iron oxide, and the sample was sonicated before deposition on the AMTIR crystal and allowing it to dry overnight. The flow cell cover was then attached, and pH-adjusted water, either pH 2 or 7, was flowed over the thin film for 30 min. A pH-adjusted solution of the ligand (1 mM) was then flowed over the surface for 100 min to investigate adsorption before pH-adjusted water was flowed over the surface for 30 to 60 min to investigate desorption. Throughout this time, spectra were collected every 5 min and averaged (range: 4000 to 750 cm^{-1}, resolution: 4 cm^{-1}).

Spectra were processed and baseline-corrected using the OMNIC software, while peak integrations were performed using Origin. The pH was measured using an Oakton pH 700 probe and calibrated using Fisher Chemical buffers at pH 1.7, 4, 7, and 10. While pH 2 ATR-FTIR experiments remained within 0.5 pH units, the pH 7 experiments exhibited more variation in pH but remained within 1.5 pH units.

Aqueous Suspension Experiments. To determine the extent of iron dissolution, as well as the potential for brown carbon formation, pH 2 experiments were carried out in 50 mL polypropylene tubes containing 16 mL solutions (0.2 mM organic compound and 0.5 mg of iron oxide/mL). While organic concentrations used in both the aqueous suspension (0.2 mM) and ATR-FTIR (1 mM) experiments were higher than those reported in field studies, typically on the order of a few μM,[36,37] higher concentrations were selected to ensure samples were within ATR-FTIR detection limits and to allow for comparisons to prior solution phase work.[25,29,30,38] Samples
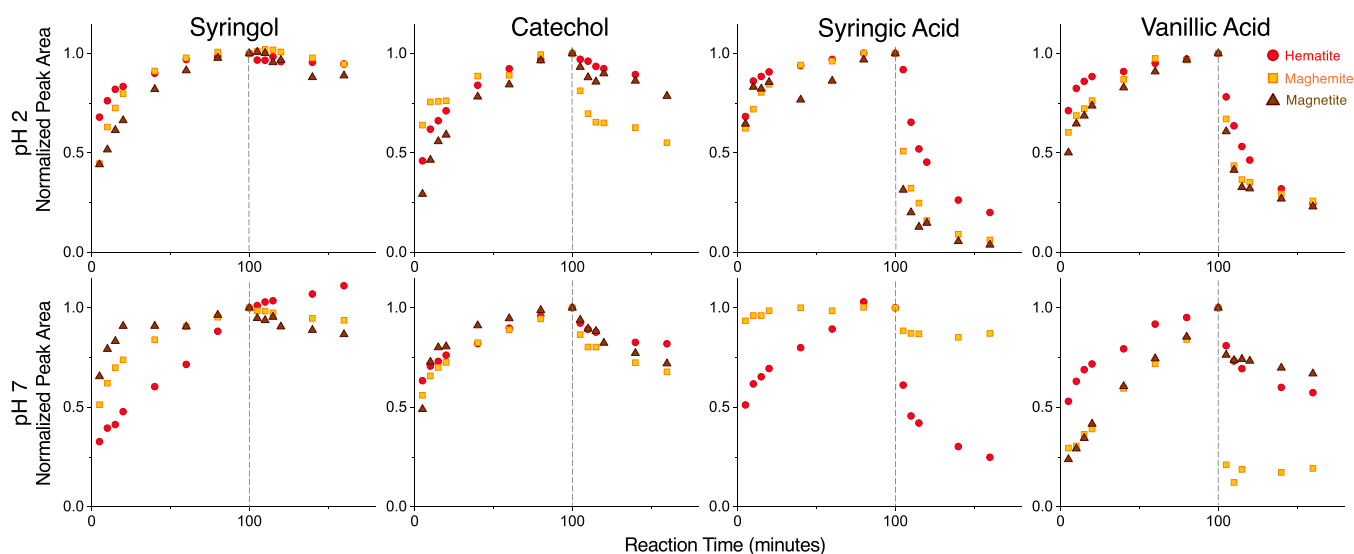
Figure 3. Normalized integrated peak areas for syringol (1277 cm^{-1}), catechol (1480 cm^{-1}), syringic acid (1116 cm^{-1}), and vanillic acid (1289 cm^{-1}) plotted as a function of experiment time. Peak area is normalized to the area at 100 min. After 100 min, pH-adjusted water (top: pH 2, bottom: pH 7) was flowed through the cell (dotted line). Peak integrations for syringic acid on magnetite under pH 7 conditions are not shown, given the lack of a clear trend.

were exposed to ambient air during preparation, and the large headspace of the tubes was chosen to ensure that samples were not oxygen-limited. Reactors were rotated end over end using a Cole−Parmer Roto-Torque heavy duty rotator at 23 rpm for 24 h in the dark before syringe filtering (Acrodisc 25 mm, 0.2 μm Supor membrane). The pH of all samples remained within 0.1 units from the initial value. UV−vis traces were collected for the filtered solution.

Fe(II) and total dissolved iron analysis were carried out using a modified Ferrozine-based colorimetric method as described in Viollier et al.[39] Briefly, 0.1 M ammonium acetate buffer and a buffered 0.01 M ferrozine solution were added to the sample, absorbance was measured, and Fe(II) determination was performed before the sample was reduced with 1.4 M hydroxylamine hydrochloride for 10 min at which point a 10 M ammonium acetate buffer (adjusted to pH 9.5) was added and the absorbance was measured again, as well as Fe(III) determination. A correction was carried to account for Fe(III) interference in the Fe(II) measurement. UV−vis measurements were carried out on a Cary 5000 UV−vis−NIR Spectrophotometer. Ferrozine (97%), ammonium acetate (99.99+%, Metals Basis), hydroxylamine hydrochloride (99.999% metals basis), hydrochloric acid (TraceMetal Grade, Fisher), and ammonium hydroxide (28% NH$_3$ in water, ≥99.99% Metals Basis) were purchased from Sigma-Aldrich. The 0.1 M ammonium acetate buffer was added to each sample directly before analysis to ensure that samples were within the pH range for the analysis (pH 4 to 9).[39] Calibration curves were prepared daily using a stock solution of Fe(III) chloride (sublimed grade, ≥99.9% trace metals basis) in a 0.01 N HCl solution. Iron content (68% α-Fe$_2$O$_3$, 71% γ-Fe$_2$O$_3$, 66% Fe$_3$O$_4$) determined during the acid digestion was used to calculate the percent dissolved iron (eq 2):

$$\frac{[\text{measured Fe}](0.016L)(55.845 \text{ g/mol})}{(\text{g iron oxide})(\text{percent iron content of oxide})} \times 100$$

$$= \text{percent dissolved iron} \qquad (2)$$

For catechol, syringol, syringic acid, and vanillic acid, ATR-FTIR measurements were carried out at both pH 2 and 7 on all three iron oxide surfaces and batch reactor experiments were conducted with all three iron oxides at pH 2. For resorcinol, guaiacol, vanillin, and levoglucosan, ATR-FTIR experiments were only carried out on maghemite surfaces at pH 2 and batch reactor experiments were only conducted with maghemite at pH 2. Aside from the use of strong acids in the digestion of the nanoparticles, no unusually high safety hazards were encountered.

■ RESULTS AND DISCUSSION

Dissolution Measurements. Dissolution experiments conducted under acidic conditions indicated that even in the absence of ligands, maghemite and magnetite released significantly more dissolved iron than hematite (Figure 1). Although it is well known that maghemite and magnetite are much more soluble than hematite,[40,41] these data nonetheless highlight the importance of using BBA-relevant iron oxide mineral phases in laboratory experiments to provide a more accurate understanding of ash dissolution in the natural environment.

Relative to the values observed in acidified water, there was a significant increase ($n = 3$, $p < 0.05$) in dissolved iron for solutions containing catechol and syringol. The observation that Fe(II) is the predominant iron oxidation state for catechol, syringol, and syringic acid illustrates that the presence of BBA-relevant ligands results in higher levels of biologically available iron.

ATR-FTIR Experiments. ATR-FTIR spectra collected for the different lignin pyrolysis products adsorbed on the three iron oxide phases at pH 2 and pH 7 showed that all four compounds formed complexes on the iron oxide surfaces; however, the intensity of the interactions and the nature of the surface species varied as discussed below (Figure 2).

The precise structure of syringol surface complexes and reductive dissolution is uncertain.[31] Krumina et al. observed the reaction of a structurally similar compound, 2,6-dimethoxy hydroquinone, at the goethite−water interface and concluded
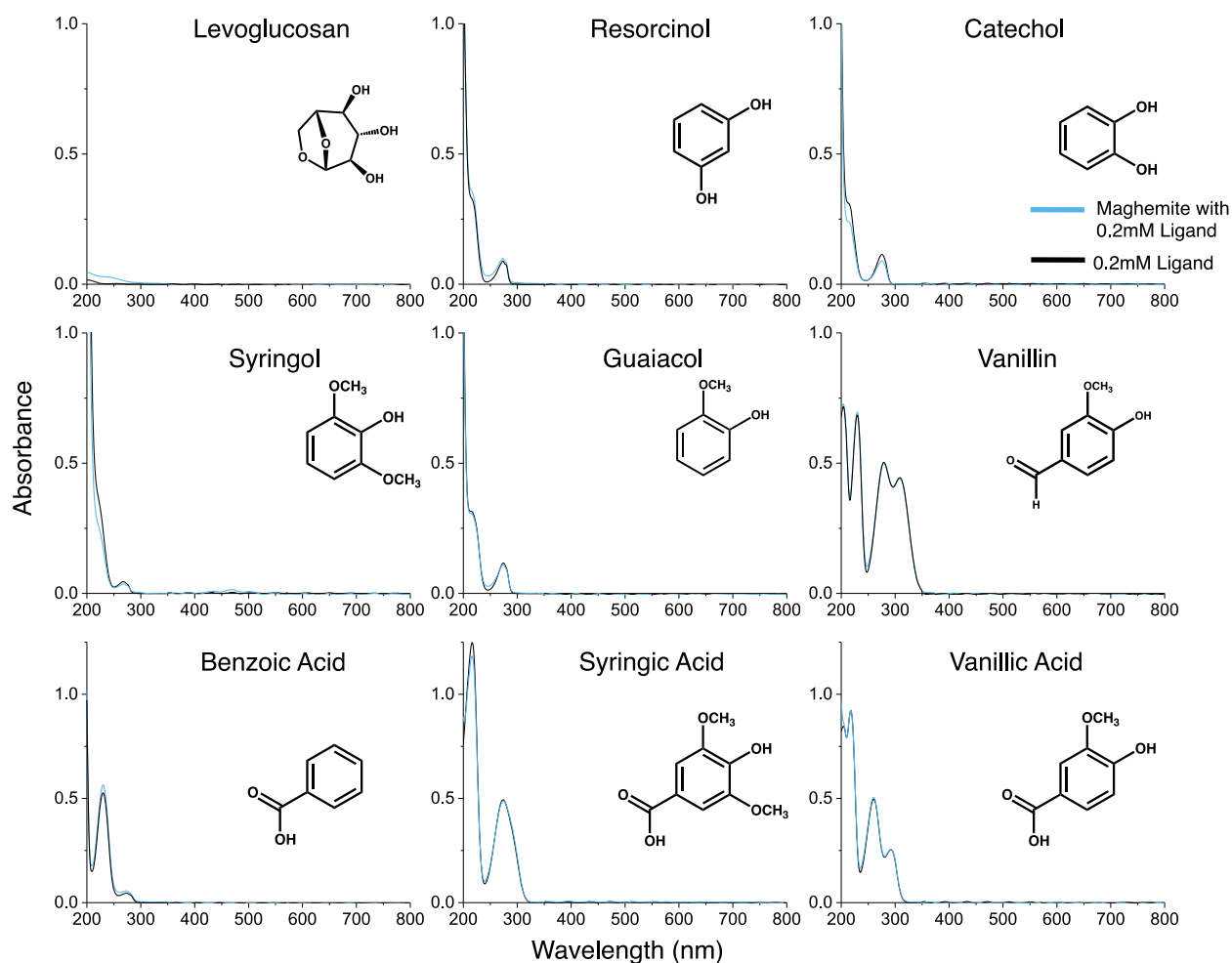
Figure 4. UV−vis spectra of the filtered batch reactors after 24 h of reaction at pH 2 with maghemite. Reactions were carried out at 0.2 mM and diluted to 0.05 mM organic concentration for spectra collection; note the change in scales for benzoic, syringic, and vanillic acids. Only the reaction of syringol leads to the formation of soluble brown carbon (peak centered around 470 nm).

that 2,6-dimethoxy hydroquinone, the semiquinone product, or another reaction product adsorbed onto the surface but that the product of reductive dissolution did not.[44] Based on the formation of an irreversibly adsorbed syringol complex observed in our experiments, we posit that syringol experiences a similar interaction with the surface as 2,6-dimethoxy hydroquinone, possibly forming a surface complex through the phenol group and a weak association with the ortho methoxy group, as evidenced by the bands at 1277 and 1259 cm^{-1} in Figure 2a−d (for complete frequency assignment, see Figure S3e,f and Table S2). This surface complex persisted throughout the desorption period, as suggested by peak integration data (Figure 3).

The formation of a surface complex was supported by the release of dissolved Fe (II), which is consistent with the reductive dissolution (Figure 1). Furthermore, the syringol dimer, which forms in the reaction of syringol with Fe (III), was detected in the aqueous experiments, as evidenced by the band at 470 nm, providing further evidence for reductive dissolution (Figure 4).[29]

Catechol formed a bidentate binuclear complex on the surface as evidenced by the peaks 1480 and 1259 cm^{-1} for all three iron oxide phases (Figure 2e−h). Prior spectroscopic and computational work has clearly showed that this type of coordination to these surfaces is favored.[45,46] A monodentate

mononuclear complex formed on the hematite surface with absorptions at 1542, 1393, and 1276 cm^{-1} (for complete frequency assignment, see Figure S3a,b and Table S3).[47−49] The formation of the monodentate mononuclear complex was unique to hematite possibly due to the smaller surface area of the hematite nanoparticles relative to the surface area of maghemite and magnetite nanoparticles (for comparisons of surface complexes as a function of concentration on all three oxide surfaces, see Figure S4). These surface complexes persisted on the surface during desorption (Figure 3). Catechol experienced a stronger interaction with the surface at pH 7, illustrated by an increase in peak intensity, in agreement with Situm et al. (2016) (Figure 2g,h).[45]

The strong interaction of catechol with the surface was associated with reductive dissolution, which was evident in the release of high concentrations of Fe(II) from the surface, and has previously been shown to occur for goethite-phenolic systems.[31]

The syringol and catechol complexes were similar at both pH values of 2 and 7. However, catechol did not form monodentate mononuclear complexes at pH 7, while syringol appeared to form some sort of product on the hematite surface during the desorption process (as evidenced by a broad peak at 1500 cm^{-1}). It was difficult to determine if the 1500 cm^{-1} peak

is evidence of a new product or related to the change in refractive index upon flowing water into the cell.

In contrast to the catechol and syringol surface complexes, the syringic and vanillic acids formed reversibly adsorbed surface complexes that were strongly pH-dependent (Figure 2i–p). At pH 2, the surfaces were fully protonated and positively charged, while at pH 7, they were deprotonated and neutrally or negatively charged.[41] Syringic acid (pK_a: 4.34) and vanillic acid (pK_a: 4.42) were protonated at pH 2 and deprotonated at pH 7.[42] At pH 2, the neutral syringic and vanillic acids experienced some interaction with the surface, likely hydrogen bonding given the weak, reversible nature of the interaction (Figure 3).[35] The peaks at 1399 (hematite) and 1393 cm^{-1} (maghemite and magnetite) are characteristic symmetric stretching vibration from the carboxylate group ($v_{s\ C-O}$) (for complete frequency assignment, see Figure S3c,d,g,h and Table S4) which suggests that the carboxylic acid group becomes deprotonated and hydrogen-bonds with the protonated surface.[50,51] At pH 7, there was little interaction between the acids and the iron oxide surfaces, and the carboxylate mode is weaker or absent, suggesting that there were no surface sites available for the acids to bind to, given that at higher pH, the surface is increasingly deprotonated.

The weaker surface interactions for both acids were further supported by the dissolved iron data. Syringic and vanillic acids lead to less dissolved iron at pH 2 than catechol and syringol. Additional experiments tracking dissolved iron release as a function of concentration indicated a significant ($n = 3$, $p < 0.05$) increase in total dissolved iron concentrations with a concentration increase from 0.05 to 0.5 mM for catechol and syringol but not for syringic or vanillic acids (Figure S5). Although all the iron present in the syringic acid experiments consisted of Fe(II) and some of the iron in the vanillic acid experiments was Fe(II) (30 to 50%), there was not a significant increase in total dissolved iron, leading us to speculate that the Fe(II) was reduced once released into the aqueous phase. The lack of a significant increase in total iron suggests that the proton-mediated dissolution was stronger than the ligand-mediated dissolution for both syringic and vanillic acids.

Variations in Surface Complexes on Magnetite Surfaces. Each ligand formed similar surface complexes on all three iron oxides; however, magnetite surfaces exhibited several peaks that were weaker or not present on the other iron oxides. For example, a negative peak observed in the magnetite–syringol sample was likely due to carbonate modes as the surface dissolved.[52] Sharp peaks were also observed for syringol on magnetite at 1627 and 1613 cm^{-1}. While these syringol peaks appeared in the maghemite experiments on magnetite, they were broader than those observed for maghemite, which could be due to the formation of additional products. However, many of the frequencies observed for magnetite in the 1700 to 1600 cm^{-1} region were challenging to assign and interpret with certainty due to the overlap with the water bending mode at approximately 1640 cm^{-1}.[53]

Magnetite and maghemite are isostructural; therefore, any differences in the surface species observed in the ATR experiments would likely be due to differences in the iron oxidation state in the minerals. The magnetite used in this study was partially oxidized (i.e., it contained approximately 14% Fe(II), but it still contained Fe(II) in the crystal lattice). To determine if the peaks were due to the presence of Fe(II)

or an impurity, the magnetite sample was heated in an oven (220 °C) for 12 h fully oxidizing the sample. ATR-FTIR experiments were carried out with this oxidized sample. The spectra of the oxidized sample were similar to those of the unoxidized sample, with the major difference being the carbonate mode (Figure S6).

It is possible for substituted aromatics to undergo reactions other than reductive dissolution at the iron interface. Krumina et al. observed the catalytic oxidation of 2,6-dimethoxy hydroquinone on goethite surfaces (eq 3) to produce a quinone and hydrogen peroxide:[44]

$$QH_2 + O_2 \xrightarrow{\text{catalyst}} Q + H_2O_2 \tag{3}$$
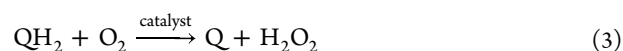
However, we do not think that syringol undergoes a catalytic reaction under the experimental conditions. Enhanced levels of total dissolved iron and Fe(II) in dissolution experiments suggest that syringol promoted reductive dissolution, leading us to hypothesize that syringol does not have sufficient electron density to undergo a catalytic reaction. However, more work is needed with probe molecules to determine if this type of catalytic reaction can occur.[54]

Soluble Brown Carbon Formation. Formation of soluble, light absorbing species (i.e., brown carbon), determined by the appearance of new peaks in the visible region (400–700 nm),[55] was only observed at 24 h in the reaction of syringol with the three iron oxides (Figure 4; for spectra with all three iron oxides, see Figure S7). Tracking reactions to 48 h showed that while the reaction was not at equilibrium at 24 h, dissolved iron concentrations continued to increase (for a plot of dissolved iron as a function of time, see Figure S8), more soluble brown carbon was not formed (for UV–vis spectra, Figure S9). The peak around 470 nm is indicative of the syringol dimer observed in previous studies.[29,30] Light-absorbing products reported in other studies after 24 h for catechol (Slikboer et al. (2015): 1.96 mM FeCl₃(aq) and 0.98 mM catechol, pH 3; Li et al. (2023): 0.4 mM FeCl₃(aq) and 0.2 mM catechol, pH 3) and guaiacol (Slikboer et al. (2015): 1 mM FeCl₃(aq) and 0.5 mM guaiacol, pH 3; Li et al. (2023): 0.4 mM FeCl₃(aq) and 0.2 mM guaiacol, pH 3) were not observed in this study.[30] In comparing this work to prior studies, it should be noted that in addition to the presence of surfaces, dissolved iron concentrations here are a factor of 3 to 15 times lower depending on the iron oxide. Additionally, the collected UV–vis traces characterize only the soluble brown carbon, as they were collected after filtering, which was not carried out in all prior studies. It is hypothesized that any brown carbon that formed underwent polymerization and that these larger, possibly more hydrophobic polymers then partitioned to the iron oxide surface or agglomerated to form particles themselves, given that catechol, syringol, and guaiacol are known to form insoluble products.[25,27,29,30] Future studies that focused on the transformation of the organic fraction using mass spectrometry would be insightful for developing a more complete understanding of the mechanism, but our results suggest that under more iron limited conditions and in the presence of surfaces, less brown carbon remains in the aqueous phase.

Competitive Adsorption for Ligand Mixtures. To test the potential for synergistic or competitive adsorption effects, we investigated the reactivity for a mixture of all four ligands (0.2 mM total ligand concentration in equal abundance for batch reactors, 1 mM total for ATR-FTIR experiments).
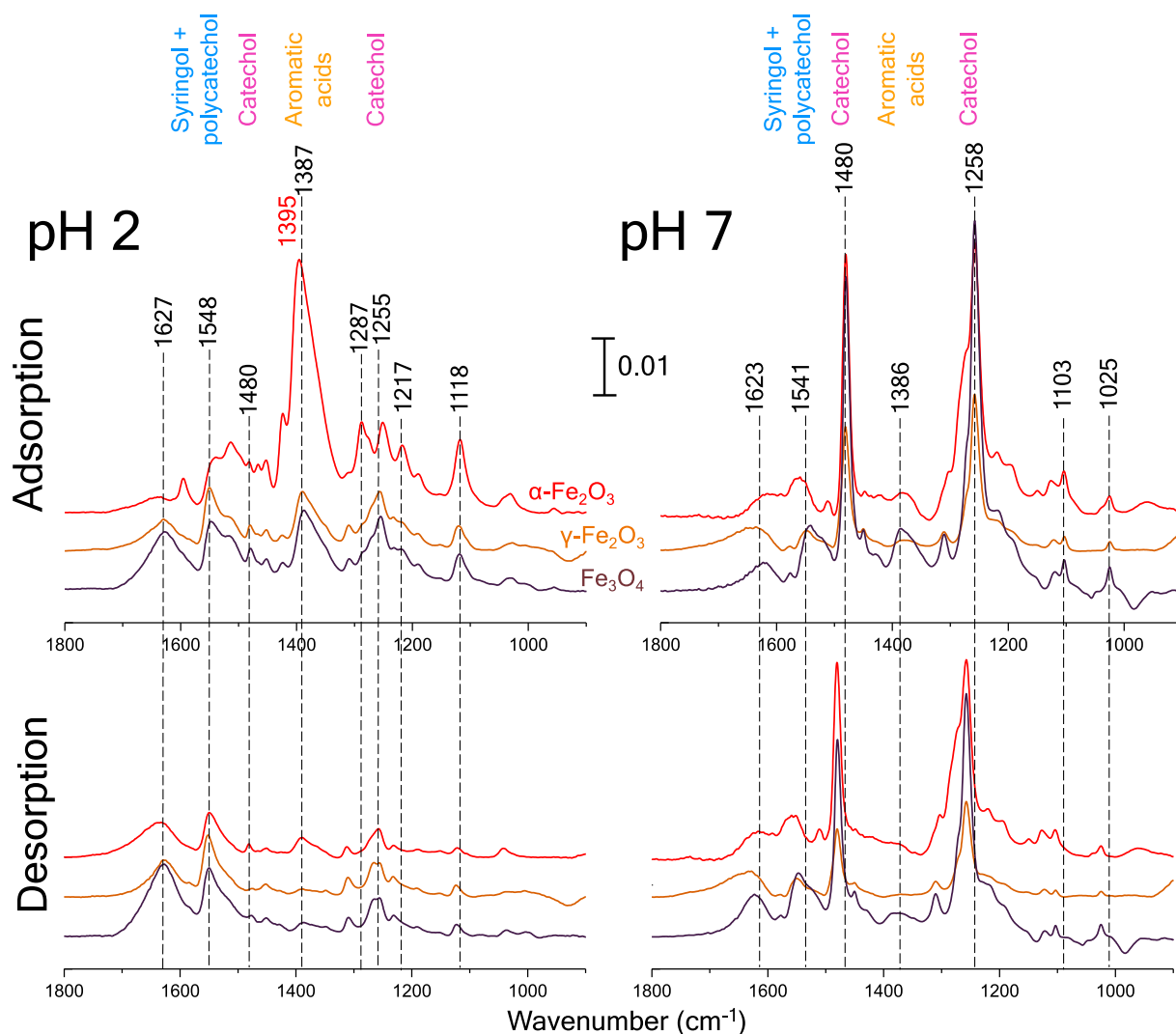
Figure 5. Top: ATR-FTIR spectra showing adsorption and 100 min of flowing 1 mM total ligand (0.05 mM catechol, syringol, syringic acid, and vanillic acid) solution over a maghemite surface at pH 2 (left) and pH 7 (right). Bottom: desorption after 60 min of flowing pH-adjusted water at pH 2 and 7, respectively. Highlighted regions indicate peak assignments.
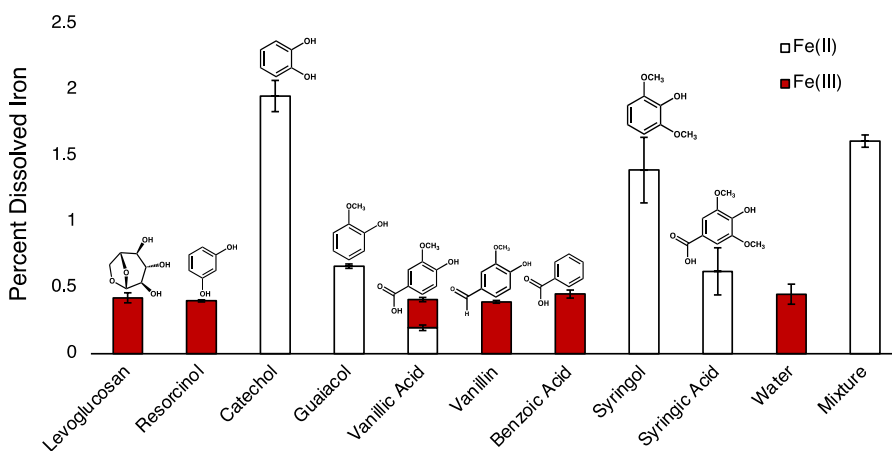

Figure 6. Percent dissolved iron after 24 h of reacting maghemite with various BBA tracer species (0.2 mM) at pH 2. Mixture indicates a sample with 0.05 mM catechol, syringol, syringic acid, and vanillic acid (0.2 mM ligand total). Vanillin Fe(II) concentrations were below LOQ.

Syringic and vanillic acids dominate the hematite spectrum at pH 2; however, for the maghemite and magnetite, the spectra exhibited a strong signal from catechol and the aromatic acids at pH 2 (Figure 5). Alone, the acids exhibited a stronger signal on the hematite surface relative to the other iron oxides (Figure 2). The observed differences between bonding on the

hematite phase versus that on maghemite and magnetite phases may arise from differences in the surface electronic structure due to metal–ligand charge transfer or other bonding effects; further study of the role of crystal facets is needed to resolve this issue.[56]

Despite the presence of the aromatic acids at the interface, reductive dissolution still occurred for all three iron oxides investigated here, leading to higher concentrations of dissolved iron and Fe(II) (for a comparison of the mixture with catechol, see Figure S10). Additionally, there was evidence at 470 nm that the syringol dimer formed, which suggests that syringol still reacted at the interface (for UV–vis spectra, see Figure S11). ATR-FTIR experiments with the mixture at pH 7 showed that catechol was the main ligand at the surface, which further emphasizes the electrostatic nature of the interactions and the importance of surface speciation and available binding sites. These competitive experiments indicate that reductive dissolution of these iron oxide phases by catechol and syringol can still occur in the presence of other compounds that exhibit high affinities for the surface.

Iron Dissolution for Other Substituted Aromatic Compounds and BBA-Relevant Ligands. To further understand how these substituted aromatic compounds impacted reductive dissolution, we investigated iron release from maghemite with several structurally similar ligands as well as other BBA relevant ligands (Figure 6).

Sufficient electron density at the phenol group was key to the formation of a surface complex and reductive dissolution to occur. When comparing the isomers catechol and resorcinol, resorcinol did not influence dissolved iron levels or lead to the reduction of iron, unlike catechol, nor did resorcinol form a surface complex (for ATR-FTIR spectra of all compounds in Figure 6 at pH 2 in the presence of a maghemite surface, see Figure S12; for a complete summary of all additional compounds, see Table S5). We hypothesize that the lack of a surface complex and reductive dissolution can be explained by a decreased electron density at the phenolic group of resorcinol. In a comparison of the isomers catechol, resorcinol, and hydroquinone at pH 3.8, LaKind and Stone showed that the rate of reductive dissolution for the three compounds, which goes as catechol ≈ hydroquinone > resorcinol, could be explained by the resonance structures of the three compounds.[31] While only catechol and resorcinol are BBA-relevant, the comparison with hydroquinone highlights the importance of ring functional groups even if they do not participate in surface complexation.

We further hypothesize that the lack of electron density can also explain the limited reductive dissolution in the presence of guaiacol and the lack of surface complex formation. Guaiacol did not interact with the iron oxide surface or lead to the same enhancement in dissolved iron levels as catechol and syringol despite having similar Lewis base ortho functionality.[57] Given the structural similarities between guaiacol and syringol but their different dissolution and complexation behaviors, we hypothesize that the second methoxy group of syringol was key to enabling reductive dissolution by increasing the electron density. The addition of electron withdrawing groups to the guaiacol structure, in the cases of vanillic acid and vanillin, further decreased the electron density and led to less reductive dissolution. The addition of an electron withdrawing group also explains the decrease in iron reduction when comparing syringol to syringic acid. Both vanillic and syringic acids have reduced reactivity relative to guaiacol and syringol and begin to

behave more like benzoic acid, which does not promote reductive dissolution.

Proxies for electron density, such as pK_a, however, do not always accurately predict the reactivity of these compounds at the interface. Aqueous phase studies also cannot accurately predict reactions at the iron oxide interface. A recent study observed a higher polymeric yield for guaiacol compared to catechol during reactions with dissolved iron, $FeCl_3$, suggesting that guaiacol was more reactive than catechol in the aqueous phase.[30] However, we found that guaiacol resulted in less dissolved iron in the presence of iron oxides than catechol, suggesting that guaiacol was less reactive at the iron oxide interface. Computational studies would be useful for accurately predicting the behavior of lignin pyrolysis products at the iron oxide interface.

Lastly, comparing these lignin pyrolysis products to levoglucosan, a BBA tracer species and cellulose combustion product,[58] demonstrates the different behavior of the two classes of biopolymer combustion products.

Environmental Significance. The reactions of lignin pyrolysis products with dissolved iron have been well studied with respect to the roles of functional groups, pH, and dissolved oxygen in polymer yield.[28,30,59,60] However, most iron within BBA is associated with solid iron oxide phases, which behave in a much different manner due to the influence of the crystal surface on the interactions between the ligand and the metal.[14,61] Furthermore, prior studies of these interactions with organic ligands focused on mineral phases that are not prevalent in BBA, such as goethite.[27,31] By studying BBA organic ligands on iron oxides under conditions that are atmospherically relevant (e.g., acidic conditions), we have found that the tendency of ligands to form surface complexes was the key indicator of the likelihood of dissolved iron release. Among the ligands studied, catechol and syringol both formed irreversibly bound surface complexes, which lead to reductive dissolution and higher concentrations of dissolved, biologically available iron for the BBA iron mineral phases. Recent modeling work has demonstrated that soluble substituted phenols, like syringol, can efficiently partition into aqueous droplets where this kind of chemistry can occur.[62] Other ligands, such as vanillic acid and levoglucosan, had little effect. Although catechol and syringol concentrations in BBA may be lower than those studied here,[36] lignin pyrolysis products with structures similar to catechol and syringol may explain the enhanced levels of dissolved iron observed in BBA, provided that they have sufficient electron density. Future research could focus on developing computational models to predict the reactivity on iron oxide surfaces. Such models could assist in determining the abundance of bioavailable iron released during atmospheric processing of BBA and thus the corresponding environmental impact.

■ ASSOCIATED CONTENT

ⓈI Supporting Information

The Supporting Information is available free of charge at https://pubs.acs.org/doi/10.1021/acsearthspacechem.4c00212.

> Characterization of iron oxide mineral phases (Section S1); ATR-FTIR experimental peak frequencies and mode sssignments (Section S2); iron dissolution as a function of ligand concentration (Section S3); reactions of organics on Fe_3O_4 and oxidized Fe_3O_4 (Section S4);

brown carbon formation (Section S5); iron dissolution in a ligand mixture (Section S6); maghemite surface experiments for additional compounds (Section S7) with Figures S1–S12 and Tables S1–S5 (PDF)

■ AUTHOR INFORMATION

Corresponding Author

Vicki H. Grassian − *Department of Chemistry and Biochemistry, University of California San Diego, La Jolla, California 92093, United States;* ⊙ orcid.org/0000-0001-5052-0045; Phone: 858-534-2499; Email: vhgrassian@ucsd.edu

Authors

Jane A. Sedlak − *Department of Chemistry and Biochemistry, University of California San Diego, La Jolla, California 92093, United States;* ⊙ orcid.org/0009-0002-9355-5736

Manal Vishnoi − *Department of Chemistry and Biochemistry, University of California San Diego, La Jolla, California 92093, United States*

Kiefer Forsch − *Geoscience Research Division, Scripps Institution of Oceanography, University of California San Diego, La Jolla, California 92093, United States*

Pazinah Bhadha − *Department of Chemistry and Biochemistry, University of California San Diego, La Jolla, California 92093, United States*

Sarah M. Aarons − *Geoscience Research Division, Scripps Institution of Oceanography, University of California San Diego, La Jolla, California 92093, United States;* ⊙ orcid.org/0000-0002-3580-0820

Complete contact information is available at:
https://pubs.acs.org/10.1021/acsearthspacechem.4c00212

Notes

The authors declare no competing financial interest.

■ ACKNOWLEDGMENTS

■ REFERENCES

(1) Burke, M.; Childs, M. L.; De La Cuesta, B.; Qiu, M.; Li, J.; Gould, C. F.; Heft-Neal, S.; Wara, M. The Contribution of Wildfire to PM2.5 Trends in the USA. *Nature* 2023, 622 (7984), 761.

(2) Ford, B.; Val Martin, M.; Zelasky, S. E.; Fischer, E. V.; Anenberg, S. C.; Heald, C. L.; Pierce, J. R. Future Fire Impacts on Smoke Concentrations, Visibility, and Health in the Contiguous United States. *GeoHealth* 2018, 2 (8), 229–247.

(3) United Nations Environment Programme Spreading like Wildfire − The Rising Threat of Extraordinary Landscape Fires. In *UNEP Rapid Response Assessment*, United Nations Environment Programme, 2022.

(4) Schneider, S. R.; Abbatt, J. P. D. Wildfire Atmospheric Chemistry: Climate and Air Quality Impacts. *Trends Chem.* 2022, 4 (4), 255–257.

(5) Schroth, A. W.; Crusius, J.; Sholkovitz, E. R.; Bostick, B. C. Iron Solubility Driven by Speciation in Dust Sources to the Ocean. *Nat. Geosci.* 2009, 2 (5), 337–340.

(6) Jahn, L. G.; Jahl, L. G.; Bland, G. D.; Bowers, B. B.; Monroe, L. W.; Sullivan, R. C. Metallic and Crustal Elements in Biomass-Burning Aerosol and Ash: Prevalence, Significance, and Similarity to Soil Particles. *ACS Earth Space Chem.* 2021, 5 (1), 136–148.

(7) Cwiertny, D. M.; Baltrusaitis, J.; Hunter, G. J.; Laskin, A.; Scherer, M. M.; Grassian, V. H. Characterization and Acid-Mobilization Study of Iron-Containing Mineral Dust Source Materials. *J. Geophys. Res.* 2008, 113, D05202.

(8) Simoneit, B. R. T. Biomass Burning — a Review of Organic Tracers for Smoke from Incomplete Combustion. *Appl. Geochem.* 2002, 17 (3), 129–162.

(9) Tang, W.; Llort, J.; Weis, J.; Perron, M. M. G.; Basart, S.; Li, Z.; Sathyendranath, S.; Jackson, T.; Sanz Rodriguez, E.; Proemse, B. C.; Bowie, A. R.; Schallenberg, C.; Strutton, P. G.; Matear, R.; Cassar, N. Widespread Phytoplankton Blooms Triggered by 2019–2020 Australian Wildfires. *Nature* 2021, 597 (7876), 370–375.

(10) Aguilera, R.; Corringham, T.; Gershunov, A.; Benmarhnia, T. Wildfire Smoke Impacts Respiratory Health More than Fine Particles from Other Sources: Observational Evidence from Southern California. *Nat. Commun.* 2021, 12 (1), 1493.

(11) Fang, T.; Hwang, B. C. H.; Kapur, S.; Hopstock, K. S.; Wei, J.; Nguyen, V.; Nizkorodov, S. A.; Shiraiwa, M. Wildfire Particulate Matter as a Source of Environmentally Persistent Free Radicals and Reactive Oxygen Species. *Environ. Sci.: Atmos.* 2023, 3 (3), 581–594.

(12) Pardo, M.; Qiu, X.; Zimmermann, R.; Rudich, Y. Particulate Matter Toxicity Is Nrf2 and Mitochondria Dependent: The Roles of Metals and Polycyclic Aromatic Hydrocarbons. *Chem. Res. Toxicol.* 2020, 33 (5), 1110–1120.

(13) Szady, C.; Picarillo, G.; Davis, E. J.; Drapanauskaite, D.; Buneviciene, K.; Baltrusaitis, J.; Navea, J. G. Iron Dissolution and Speciation from Combustion Particles under Environmentally Relevant Conditions. *Environ. Chem.* 2023, 20, 171–182.

(14) Paris, R.; Desboeufs, K. V.; Formenti, P.; Nava, S.; Chou, C. Chemical Characterisation of Iron in Dust and Biomass Burning Aerosols during AMMA-SOP0/DABEX: Implication for Iron Solubility. *Atmos. Chem. Phys.* 2010, 10 (9), 4273–4282.

(15) Perron, M. M. G.; Proemse, B. C.; Strzelec, M.; Gault-Ringold, M.; Boyd, P. W.; Sanz Rodriguez, E.; Paull, B.; Bowie, A. R. Origin, transport and deposition of aerosol iron to Australian coastal waters. *Atmos. Environ.* 2020, 228 (117432), 117432.

(16) Oakes, M.; Ingall, E. D.; Lai, B.; Shafer, M. M.; Hays, M. D.; Liu, Z. G.; Russell, A. G.; Weber, R. J. Iron Solubility Related to Particle Sulfur Content in Source Emission and Ambient Fine Particles. *Environ. Sci. Technol.* 2012, 46 (12), 6637–6644.

(17) Hamilton, D. S.; Perron, M. M. G.; Bond, T. C.; Bowie, A. R.; Buchholz, R. R.; Guieu, C.; Ito, A.; Maenhaut, W.; Myriokefalitakis, S.; Olgun, N.; et al. Earth, Wind, Fire, and Pollution: Aerosol Nutrient Sources and Impacts on Ocean Biogeochemistry. *Annu. Rev. Mar. Sci.* 2022, 14 (1), 303–330.

(18) Sedwick, P. N.; Sholkovitz, E. R.; Church, T. M. Impact of Anthropogenic Combustion Emissions on the Fractional Solubility of Aerosol Iron: Evidence from the Sargasso Sea. *Geochem., Geophys., Geosyst.* 2007, 8 (10), 2007GC001586.

(19) Ito, A.; Ye, Y.; Baldo, C.; Shi, Z. Ocean Fertilization by Pyrogenic Aerosol Iron. *Npj Clim. Atmos. Sci.* 2021, 4 (1), 30.

(20) Tegler, L. A.; Sherry, A. M.; Herckes, P.; Romaniello, S. J.; Anbar, A. D. Up in Smoke: Most Aerosolized Fe From Biomass Burning Does Not Derive From Foliage. *Global Biogeochem. Cycles* 2023, 37 (9), No. e2023GB007796.

(21) Lopez, A. M.; Avila, C. C. E.; VanderRoest, J. P.; Roth, H. K.; Fendorf, S.; Borch, T. Molecular Insights and Impacts of Wildfire-Induced Soil Chemical Changes. *Nat. Rev. Earth Environ.* 2024, 5, 431.

(22) Baalousha, M.; Desmau, M.; Singerling, S. A.; Webster, J. P.; Matiasek, S. J.; Stern, M. A.; Alpers, C. N. Discovery and Potential Ramifications of Reduced Iron-Bearing Nanoparticles—Magnetite,

Wüstite, and Zero-Valent Iron—in Wildland—Urban Interface Fire Ashes. *Environ. Sci.: Nano* 2022, 9 (11), 4136−4149.

(23) Goforth, B. R.; Graham, R. C.; Hubbert, K. R.; Zanner, C. W.; Minnich, R. A. Spatial Distribution and Properties of Ash and Thermally Altered Soils after High-Severity Forest Fire, Southern California. *Int. J. Wildland Fire* 2005, 14 (4), 343.

(24) Jordanova, N.; Jordanova, D.; Barrón, V. Wildfire Severity: Environmental Effects Revealed by Soil Magnetic Properties. *Land Degrad. Dev.* 2019, 30 (18), 2226−2242.

(25) Slikboer, S.; Grandy, L.; Blair, S. L.; Nizkorodov, S. A.; Smith, R. W.; Al-Abadleh, H. A. Formation of Light Absorbing Soluble Secondary Organics and Insoluble Polymeric Particles from the Dark Reaction of Catechol and Guaiacol with Fe(III). *Environ. Sci. Technol.* 2015, 49 (13), 7793−7801.

(26) Hopstock, K. S.; Carpenter, B. P.; Patterson, J. P.; Al-Abadleh, H. A.; Nizkorodov, S. A. Formation of Insoluble Brown Carbon through Iron-Catalyzed Reaction of Biomass Burning Organics. *Environ. Sci.: Atmos.* 2023, 3 (1), 207−220.

(27) Link, N.; Removski, N.; Yun, J.; Fleming, L. T.; Nizkorodov, S. A.; Bertram, A. K.; Al-Abadleh, H. A. Dust-Catalyzed Oxidative Polymerization of Catechol and Its Impacts on Ice Nucleation Efficiency and Optical Properties. *ACS Earth Space Chem.* 2020, 4 (7), 1127−1139.

(28) Chin, H.; Hopstock, K. S.; Fleming, L. T.; Nizkorodov, S. A.; Al-Abadleh, H. A. Effect of Aromatic Ring Substituents on the Ability of Catechol to Produce Brown Carbon in Iron (III)-Catalyzed Reactions. *Environ. Sci.: Atmos.* 2021, 1 (2), 64−78.

(29) Lavi, A.; Lin, P.; Bhaduri, B.; Carmieli, R.; Laskin, A.; Rudich, Y. Characterization of Light-Absorbing Oligomers from Reactions of Phenolic Compounds and Fe(III). *ACS Earth Space Chem.* 2017, 1 (10), 637−646.

(30) Li, F.; Tang, S.; Lv, J.; He, A.; Wang, Y.; Liu, S.; Cao, H.; Zhao, L.; Wang, Y.; Jiang, G. Molecular-Scale Investigation on the Formation of Brown Carbon Aerosol via Iron-Phenolic Compound Reactions in the Dark. *Environ. Sci. Technol.* 2023, 57, 11173.

(31) LaKind, J. S.; Stone, A. T. Reductive Dissolution of Goethite by Phenolic Reductants. *Geochim. Cosmochim. Acta* 1989, 53 (5), 961−971.

(32) Sit, I.; Young, M. A.; Kubicki, J. D.; Grassian, V. H. Distinguishing Different Surface Interactions for Nucleotides Adsorbed onto Hematite and Goethite Particle Surfaces through ATR-FTIR Spectroscopy and DFT Calculations. *Phys. Chem. Chem. Phys.* 2023, 25 (30), 20557−20566.

(33) Sit, I.; Quirk, E.; Hettiarachchi, E.; Grassian, V. H. Differential Surface Interactions and Surface Templating of Nucleotides (dGMP, dCMP, dAMP, and dTMP) on Oxide Particle Surfaces. *Langmuir* 2022, 38, 15038.

(34) Kim, D.; Grassian, V. H. Attenuated Total Reflection-Fourier Transform Infrared and Atomic Force Microscopy-Infrared Spectroscopic Investigation of Suwannee River Fulvic Acid and Its Interactions with α-FeOOH. *ACS Earth Space Chem.* 2022, 6 (1), 81−89.

(35) Sit, I.; Wu, H.; Grassian, V. H. Environmental Aspects of Oxide Nanoparticles: Probing Oxide Nanoparticle Surface Processes Under Different Environmental Conditions. *Annual Rev. Anal. Chem.* 2021, 14 (1), 489−514.

(36) Anastasio, C.; Faust, B. C.; Rao, C. J. Aromatic Carbonyl Compounds as Aqueous-Phase Photochemical Sources of Hydrogen Peroxide in Acidic Sulfate Aerosols, Fogs, and Clouds. 1. Non-Phenolic Methoxybenzaldehydes and Methoxyacetophenones with Reductants (Phenols). *Environ. Sci. Technol.* 1997, 31 (1), 218−232.

(37) Sagebiel, J. C.; Seiber, J. N. Studies on the Occurrence and Distribution of Wood Smoke Marker Compounds in Foggy Atmospheres. *Environ. Toxicol. Chem.* 1993, 12 (5), 813−822.

(38) Xu, J.; Cui, T.; Fowler, B.; Fankhauser, A.; Yang, K.; Surratt, J. D.; McNeill, V. F. Aerosol Brown Carbon from Dark Reactions of Syringol in Aqueous Aerosol Mimics. *ACS Earth Space Chem.* 2018, 2 (6), 608−617.

(39) Viollier, E.; Inglett, P. W.; Hunter, K.; Roychoudhury, A. N.; Van Cappellen, P. The Ferrozine Method Revisited: Fe(II)/Fe(III) Determination in Natural Waters. *Appl. Geochem.* 2000, 15 (6), 785−790.

(40) Sidhu, P. S.; Gilkes, R. J.; Cornell, R. M.; Posner, A. M.; Quirk, J. P. Dissolution of Iron Oxides and Oxyhydroxides in Hydrochloric and Perchloric Acids. *Clays Clay Miner.* 1981, 29 (4), 269−276.

(41) Cornell, R. M.; Schwertmann, U. *The Iron Oxides: Structure, Properties, Reactions, Occurrences, and Uses*, Wiley-VCH, 2003.

(42) Ragnar, M.; Lindgren, C. T.; Nilvebrant, N.-O. pKa Values of Guaiacyl and Syringyl Phenols Related to Lignin. *J. Wood Chem. Technol.* 2000, 20 (3), 277−305.

(43) Schweigert, N.; Zehnder, A. J. B.; Eggen, R. I. L. Chemical Properties of Catechols and Their Molecular Modes of Toxic Action in Cells, from Microorganisms to Mammals: Minireview. *Environ. Microbiol.* 2001, 3 (2), 81−91.

(44) Krumina, L.; Lyngsie, G.; Tunlid, A.; Persson, P. Oxidation of a Dimethoxyhydroquinone by Ferrihydrite and Goethite Nanoparticles: Iron Reduction versus Surface Catalysis. *Environ. Sci. Technol.* 2017, 51 (16), 9053−9061.

(45) Situm, A.; Rahman, M. A.; Goldberg, S.; Al-Abadleh, H. A. Spectral Characterization and Surface Complexation Modeling of Low Molecular Weight Organics on Hematite Nanoparticles: Role of Electrolytes in the Binding Mechanism. *Environ. Sci.: Nano* 2016, 3 (4), 910−926.

(46) Augustine, L. J.; Abbaspour Tamijani, A.; Bjorklund, J. L.; Al-Abadleh, H. A.; Mason, S. E. Adsorption of Small Organic Acids and Polyphenols on Hematite Surfaces: Density Functional Theory + Thermodynamics Analysis. *J. Colloid Interface Sci.* 2022, 609, 469−481.

(47) Yang, Y.; Yan, W.; Jing, C. Dynamic Adsorption of Catechol at the Goethite/Aqueous Solution Interface: A Molecular-Scale Study. *Langmuir* 2012, 28 (41), 14588−14597.

(48) Tofan-Lazar, J.; Situm, A.; Al-Abadleh, H. A. DRIFTS Studies on the Role of Surface Water in Stabilizing Catechol−Iron(III) Complexes at the Gas/Solid Interface. *J. Phys. Chem. A* 2013, 117 (40), 10368−10380.

(49) Gulley-Stahl, H.; Hogan, P. A.; Schmidt, W. L.; Wall, S. J.; Buhrlage, A.; Bullen, H. A. Surface Complexation of Catechol to Metal Oxides: An ATR-FTIR, Adsorption, and Dissolution Study. *Environ. Sci. Technol.* 2010, 44 (11), 4116−4121.

(50) Dobson, K. D.; McQuillan, A. J. In Situ Infrared Spectroscopic Analysis of the Adsorption of Aromatic Carboxylic Acids to TiO2, ZrO2, Al2O3, and Ta2O5 from Aqueous Solutions. *Spectrochim. Acta, Part A* 2000, 56 (3), 557−565.

(51) Norén, K.; Persson, P. Adsorption of Monocarboxylates at the Water/Goethite Interface: The Importance of Hydrogen Bonding. *Geochim. Cosmochim. Acta* 2007, 71 (23), 5717−5730.

(52) Baltrusaitis, J.; Grassian, V. H. Surface Reactions of Carbon Dioxide at the Adsorbed Water−Iron Oxide Interface. *J. Phys. Chem. B* 2005, 109 (25), 12227−12230.

(53) Sit, I.; Sagisaka, S.; Grassian, V. H. Nucleotide Adsorption on Iron(III) Oxide Nanoparticle Surfaces: Insights into Nano−Geo−Bio Interactions Through Vibrational Spectroscopy. *Langmuir* 2020, 36 (51), 15501−15513.

(54) Lyngsie, G.; Krumina, L.; Tunlid, A.; Persson, P. Generation of Hydroxyl Radicals from Reactions between a Dimethoxyhydroquinone and Iron Oxide Nanoparticles. *Sci. Rep.* 2018, 8 (1), 10834.

(55) Laskin, A.; Laskin, J.; Nizkorodov, S. A. Chemistry of Atmospheric Brown Carbon. *Chem. Rev.* 2015, 115 (10), 4335−4382.

(56) Mäkie, P.; Westin, G.; Persson, P.; Österlund, L. Adsorption of Trimethyl Phosphate on Maghemite, Hematite, and Goethite Nanoparticles. *J. Phys. Chem. A* 2011, 115 (32), 8948−8959.

(57) Vasudevan, D.; Stone, A. T. Adsorption of Catechols, 2-Aminophenols, and 1,2-Phenylenediamines at the Metal (Hydr)-Oxide/Water Interface: Effect of Ring Substituents on the Adsorption onto TiO 2. *Environ. Sci. Technol.* 1996, 30 (5), 1604−1613.

(58) Suciu, L. G.; Masiello, C. A.; Griffin, R. J. Anhydrosugars as Tracers in the Earth System. *Biogeochemistry* 2019, 146 (3), 209−256.

(59) Al-Abadleh, H. A.; Motaghedi, F.; Mohammed, W.; Rana, M. S.; Malek, K. A.; Rastogi, D.; Asa-Awuku, A. A.; Guzman, M. I. Reactivity of Aminophenols in Forming Nitrogen-Containing Brown Carbon from Iron-Catalyzed Reactions. *Commun. Chem.* **2022**, *5* (1), 112.

(60) Al-Abadleh, H. A. Aging of Atmospheric Aerosols and the Role of Iron in Catalyzing Brown Carbon Formation. *Environ. Sci.: Atmos.* **2021**, *1* (6), 297−345.

(61) Guieu, C.; Bonnet, S.; Wagener, T.; Loÿe-Pilot, M. Biomass Burning as a Source of Dissolved Iron to the Open Ocean? *Geophys. Res. Lett.* **2005**, *32* (19), 2005GL022962.

(62) Zhang, J.; Shrivastava, M.; Ma, L.; Jiang, W.; Anastasio, C.; Zhang, Q.; Zelenyuk, A. Modeling Novel Aqueous Particle and Cloud Chemistry Processes of Biomass Burning Phenols and Their Potential to Form Secondary Organic Aerosols. *Environ. Sci. Technol.* **2024**, *58*, 3776.